J. Fluid Mech. (2012), *vol.* 703, *pp.* 29–48.
doi:10.1017/jfm.2012.183

Evolution of a stratified rotating shear layer with horizontal shear. Part I. Linear stability

Eric Arobone and Sutanu Sarkar†

Department of Mechanical and Aerospace Engineering, University of California San Diego, CA 92093, USA

(Received 28 June 2011; revised 22 February 2012; accepted 12 April 2012; first published online 13 June 2012)

Linear stability analysis is used to investigate instability mechanisms for a horizontally oriented hyperbolic tangent mixing layer with uniform stable stratification and coordinate system rotation about the vertical axis. The important parameters governing inviscid dynamics are maximum shear S, buoyancy frequency N, angular velocity of rotation Ω and characteristic shear thickness L. Growth rates associated with the most unstable modes are explored as a function of stratification strength N/S and rotation strength $2\Omega/S$. In the case of strong stratification, growth rates exhibit self-similarity of the form $\sigma(k_1L, Sk_3L/N, 2\Omega/S)$. In the case of rapid rotation we also observe self-similar scaling of growth rates with respect to the vertical wavenumber and rotation rate. The unstratified cases show $\sigma(k_1L, 2|\tilde{\Omega}|k_3L/S)$ dependence while the strongly stratified cases show $\sigma(k_1L, 2|\tilde{\Omega}|k_3L/N)$ dependence where $\tilde{\Omega}$ represents the difference between the angular velocity of rotation and least stable anticyclonic angular velocity, $\Omega = S/4$. Stratification was found to stabilize the inertial instability for weak anticyclonic rotation rates. Near the zero absolute vorticity state, stratification and rotation couple in a destabilizing manner increasing the range of unstable vertical wavenumbers associated with barotropic instability. In the case of rapid rotation, stratification prevents the stabilization of low k_1, high k_3 modes that occurs in a homogeneous fluid. The structure of certain unstable eigenmodes and the coupling between horizontal vorticity and density fluctuations are explored to explain how buoyancy stabilizes or destabilizes inertial and barotropic modes.

Key words: rotating flows, stratified flows

1. Introduction

The effects of strong stratification, where $Fr_h = S/N \lesssim O(1)$, and moderate rotation rates, where $|Ro| = S/2|\Omega| \sim O(1)$, on shear flow are important for basic understanding of submesoscale ocean dynamics. We concentrate our study on a horizontally oriented hyperbolic tangent mixing layer including stable stratification and rotation effects. Isolated horizontal shear is prevalent in boundary currents and in the wake of isolated topography. Previous work has explored the three-dimensional linear stability of a horizontally oriented shear layer subjected to rotation or stratification alone, but not in combination. Figure 1 gives a schematic illustrating the rotating stratified horizontal shear layer and relevant dimensional parameters.

† Email address for correspondence: ssarkar@ucsd.edu

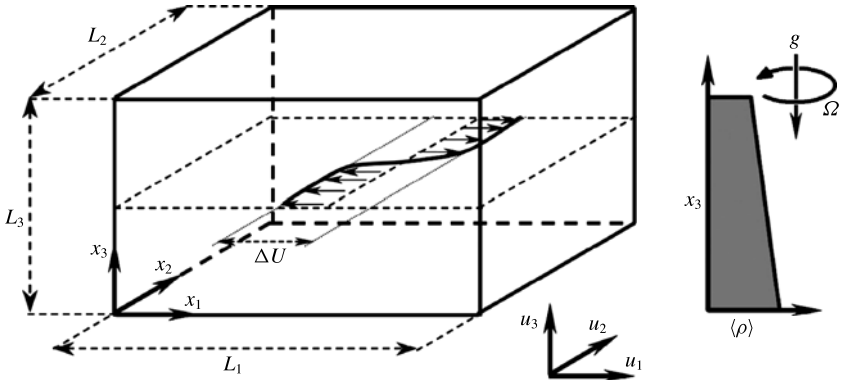

FIGURE 1. Schematic of the rotating stratified horizontal shear layer. Relevant parameters include the vorticity thickness $\delta_\omega = \Delta U/|\langle\omega_3\rangle|_{max}$, kinematic viscosity ν, mass diffusivity κ and reference density ρ_0. Cyclonic rotation refers to cases where $\langle\omega_3\rangle$ and Ω have the same sign, while anticyclonic rotation refers to cases where they have opposite signs.

Deloncle, Chomaz & Billant (2007) explored the influence of uniform stable stratification on the linear stability of a non-rotating horizontal hyperbolic tangent mixing layer with shear concentrated in a region with characteristic length scale L. When stratification was strong, with $Fr_h \lesssim 1$, self-similarity of growth rates with respect to vertical wavenumber was realized with associated scale $Fr_h k_3 L$, as opposed to the unstratified scale $k_3 L$. This result is consistent with the self-similarity of strongly stratified flows proposed by Billant & Chomaz (2001) and implies that a wider range of vertical wavenumbers are unstable when stratification is strong.

Johnson (1963) explored the effects of vertical shear $U_1(x_3)$, subjected to coordinate system rotation about an axis oriented at an arbitrary angle θ with respect to the streamwise direction. Neutral modes were computed for a hyperbolic tangent mean velocity profile for various values of θ. A horizontally oriented shear layer subjected to vertical rotation without stratification is equivalent to the $\theta = \pm 90^\circ$ cases investigated by Johnson (1963). Rotation was found to stabilize the flow, except for the anticyclonic case with $0 < 2\Omega < \mathrm{d}U_1/\mathrm{d}x_3$ where the effect of rotation was destabilizing. This result is consistent with the Rayleigh criterion for inertial instability (e.g. Holton 1992), which states that $2\Omega\,(2\Omega + \omega_3) < 0$ implies instability. Here, ω_3 is the relative vertical vorticity and $2\Omega + \omega_3$ is the corresponding absolute vertical vorticity.

The stability of a viscous hyperbolic tangent mixing layer subjected to rigid-body rotation perpendicular to the plane of the mean flow was explored by Yanase *et al.* (1993). Two distinct instability regimes were observed. The first region corresponded to the barotropic (or Kelvin–Helmholtz) instability with its growth rate peaking when $k_1 = 0.43$ and $k_3 = 0$. The second region corresponded to the inertial (or shear/Coriolis) instability with its growth rate peaking when $k_1 = 0$ and k_3 is large in comparison with barotropic modes. The neutral curves found in Johnson (1963) were determined to be incorrect and did not capture the inertial instability regime properly.

Smyth & Peltier (1994) explored the evolution of a rotating and unstratified barotropic shear layer and the stability of the temporally evolving two-dimensional flow with respect to three-dimensional perturbations. The evolution included Kelvin–Helmholtz vortex formation and pairing. Slow rotation rates either stabilized

or destabilized the barotropic vortices depending on the sign of f, while rapid rotation stabilized the flow. When the absolute vorticity was small in comparison to the relative vorticity, the vortex core was destabilized. Later, Smyth & McWilliams (1998) explored the instability of a single columnar vortex in a rotating and stratified fluid. In the case of rapid rotation and strong stratification, instability was restricted to a band of vertical wavenumbers such that $k_3 L \sim |N/f|$, consistent with quasi-geostrophy. A surprising result was that this scaling was realized outside of the formal quasi-geostrophic regime, when coordinate system rotation rates were only a few times faster than vortex core rotation rates. Inertial instability was realized for moderate anticyclonic rotation rates.

Numerical simulations of the inertial instability for various wall-bounded and free-shear flows were explored by Kloosterziel, Orlandi & Carnevale (2007). Simulations were invariant in the streamwise direction, so that the barotropic instability would not influence evolution. It was observed that the inertial instability redistributes linear momentum in a manner that yields an inertially stable final state, suppressing regions of negative potential vorticity.

Plougonven & Zeitlin (2009) investigated the development of inertial instability for a hyperbolic tangent mixing layer in a rotating stratified fluid. The barotropic instability was ignored by exploring modes that were invariant in the streamwise direction. Analytical solutions for the linear stability of the problem were derived in addition to exploration of nonlinear evolution of inertial instability and the fluctuating baroclinicity of the final state. For inviscid flow, growth rates were shown analytically to tend towards maximal values when $k_3 \to \infty$. The expression also allowed for easy computation of the most unstable vertical wavenumber for inertially unstable viscous flows. Previous investigations into the vertical scale selection associated with inertial instability include Dunkerton (1981), Griffiths (2003) and Kloosterziel & Carnevale (2008). Dunkerton (1981) and Griffiths (2003) both focused on zonal equatorial flows with the former exploring the scale selection for linear disturbances, and the latter exploring nonlinear scale selection. Griffiths observed a secondary Kelvin–Helmholtz instability which increased the vertical length scale in comparison to the linear scale. Kloosterziel & Carnevale (2008) explored a zonal flow in an f-plane as opposed to the equatorial β-plane. For large Re, the preferred vertical wavenumber was found to scale as $k_3 \propto Re^{1/3}$.

The three-dimensional stability of a Kármán vortex sheet, symmetric double row, and single row of vortices was explored in a stratified and rotating fluid by Deloncle, Billant & Chomaz (2011). For the non-rotating stratified Kármán vortex sheet, zigzag-type instabilities were realized for sufficiently close vortex rows. When rotational effects were included, cyclonic vortices were found to have less bend than anticyclonic vortices. In the rapid rotation regime, growth rates were found scale like $Ro/(bFr_h)$ where b denotes spacing between adjacent vortices in the same row. The result is consistent with quasi-geostrophic scaling laws.

In this paper, the stability of the horizontal mixing layer is explored with the influence of both stratification and rotation for fully three-dimensional perturbations. In § 2 we formulate the eigenvalue problem. In § 3 we introduce theory related to horizontal vorticity fluctuations to aid in explaining the stability of the shear layer. In § 4 we explore the effects of stratification and rotation on eigenvalues to infer various asymptotic regimes of the flow. Lastly, in § 5 we explore the effects of stratification and rotation on eigenmodes and their underlying vortex dynamics with a focus on buoyancy effects.

2. Formulation

The governing equations for Boussinesq incompressible flow in a rotating coordinate system are given here with dimensional quantities denoted by superscript *:

$$\frac{\partial u_i^*}{\partial t^*} + u_j^* \frac{\partial u_i^*}{\partial x_j^*} + \epsilon_{i3k} 2\Omega^* u_k^* = -\frac{1}{\rho_0^*}\frac{\partial p^*}{\partial x_i^*} - \frac{\rho^* g^*}{\rho_0^*}\delta_{i3} + \nu^* \frac{\partial^2 u_i^*}{\partial x_j^* \partial x_j^*}, \tag{2.1}$$

$$\frac{\partial u_i^*}{\partial x_i^*} = 0, \tag{2.2}$$

$$\frac{\partial \rho^*}{\partial t^*} + u_j^* \frac{\partial \rho^*}{\partial x_j^*} = \kappa^* \frac{\partial^2 \rho^*}{\partial x_j^* \partial x_j^*}. \tag{2.3}$$

The base state of interest is a barotropic hyperbolic tangent mixing layer of the form

$$\langle u_1^* \rangle = \frac{\Delta U^*}{2} \tanh\left(\frac{2x_2^*}{\delta_\omega^*}\right), \tag{2.4}$$

with linear vertical stratification $\mathrm{d}\langle\rho^*\rangle/\mathrm{d}x_3^*$, Coriolis parameter $f^* = 2\Omega^*$, vorticity thickness δ_ω^* and velocity difference ΔU^* as seen in figure 1. The mean pressure field is chosen to exactly balance the effects of the mean Coriolis terms and the mean buoyancy term from the momentum equations. The non-dimensional governing equations and associated non-dimensional parameters and variables are as follows:

$$\frac{\partial u_i}{\partial t} + u_j \frac{\partial u_i}{\partial x_j} + \epsilon_{i3k} 2\Omega u_k = -\frac{\partial p}{\partial x_i} - Ri_b \rho \delta_{i3} + \frac{1}{Re}\frac{\partial^2 u_i}{\partial x_j \partial x_j}, \tag{2.5}$$

$$\frac{\partial u_i}{\partial x_i} = 0, \tag{2.6}$$

$$\frac{\partial \rho}{\partial t} + u_j \frac{\partial \rho}{\partial x_j} = \frac{1}{RePr}\frac{\partial^2 \rho}{\partial x_j \partial x_j}, \tag{2.7}$$

$$Ri_b = -\frac{g^*}{\rho_0^*}\frac{\mathrm{d}\langle\rho^*\rangle}{\mathrm{d}x_3^*}\frac{\delta_\omega^{*2}}{\Delta U^{*2}} = \frac{N^{*2}\delta_\omega^{*2}}{\Delta U^{*2}} = Fr_h^{-2}, \quad 2\Omega = Ro^{-1} = \frac{f^*\delta_\omega^*}{\Delta U^*}, \tag{2.8}$$

$$Re = \frac{\Delta U^* \delta_\omega^*}{\nu^*}, \quad Pr = \frac{\nu^*}{\kappa^*}, \tag{2.9}$$

$$u_i = \frac{u_i^*}{\Delta U^*}, \quad p = \frac{p^*}{\rho_0^* \Delta U^{*2}}, \quad \rho = \frac{-\rho^*}{\delta_\omega^* \, \mathrm{d}\langle\rho^*\rangle/\mathrm{d}x_3^*}. \tag{2.10}$$

Next, linearized evolution equations are derived for small amplitude perturbations and given here:

$$\frac{\partial u_i'}{\partial t} + \langle u_1 \rangle \frac{\partial u_i'}{\partial x_1} + u_2' \frac{\mathrm{d}\langle u_i \rangle}{\mathrm{d}x_2}\delta_{i1} + \epsilon_{i3k} 2\Omega u_k' = -\frac{\partial p'}{\partial x_i} - Ri_b \rho' \delta_{i3} + \frac{1}{Re}\frac{\partial^2 u_i'}{\partial x_j \partial x_j}, \tag{2.11}$$

$$\frac{\partial u_i'}{\partial x_i} = 0, \tag{2.12}$$

$$\frac{\partial \rho'}{\partial t} + \langle u_1 \rangle \frac{\partial \rho'}{\partial x_1} - u_3' = \frac{1}{RePr}\frac{\partial^2 \rho'}{\partial x_j \partial x_j}. \tag{2.13}$$

Solutions are assumed to be wavelike in the streamwise and vertical directions with the following functional form:

$$\left[u_i', p', \rho'\right](x_2) \exp\left(\mathrm{i}k_1 x_1 + \mathrm{i}k_3 x_3 + \sigma t\right). \tag{2.14}$$

Substituting into the linearized equations of motion and combining equations in a manner similar to Deloncle *et al.* (2007), we obtain a generalized eigenvalue problem of the following form after eliminating u_3' and p' as variables:

$$\boldsymbol{A}\begin{pmatrix} u_1' \\ u_2' \\ \rho' \end{pmatrix} = \sigma \boldsymbol{B}\begin{pmatrix} u_1' \\ u_2' \\ \rho' \end{pmatrix}. \tag{2.15}$$

The matrices $\boldsymbol{A}$ and $\boldsymbol{B}$ are shown in the following equations where $k^2 = k_1^2 + k_3^2$, $\mathrm{D} = \mathrm{d}/\mathrm{d}x_2$, $\Delta = \mathrm{D}^2 - k^2$, $U = \langle u_1 \rangle$, $\nu = Re^{-1}$ and $\kappa = (RePr)^{-1}$ are used for compactness:

$$\boldsymbol{A} = \begin{bmatrix} -2\Omega k^2 & \mathrm{i}k_1\left\{U\Delta - \mathrm{D}^2 U + 2\Omega \mathrm{D}\right\} + \nu\Delta & -\mathrm{i}k_3 Ri_b \mathrm{D} \\ \mathrm{i}k_1\left(\mathrm{D}U + U\mathrm{D} - 2\Omega\right) - \nu\Delta\mathrm{D} & \mathrm{D}^2 U + k_1^2 U + \mathrm{D}U\mathrm{D} - 2\Omega\mathrm{D} + \nu \mathrm{i}k_1\Delta & 0 \\ -\mathrm{i}k_1 & -\mathrm{D} & k_1 k_3 U + \kappa \mathrm{i}k_3 \Delta \end{bmatrix} \tag{2.16}$$

$$\boldsymbol{B} = \begin{bmatrix} 0 & -\Delta & 0 \\ -\mathrm{D} & \mathrm{i}k_1 & 0 \\ 0 & 0 & \mathrm{i}k_3 \end{bmatrix}. \tag{2.17}$$

Matrices $\boldsymbol{A}$ and $\boldsymbol{B}$ are discretized using rational Chebyshev basis functions. The generalized eigenvalue problem is solved using the Intel MKL library and Fortran. Since k_3 appears in the equations only as k_3^2 or $k_3\rho'$ (which can be absorbed by definition into a new variable $k_3\rho'$) it is clear that the sign of k_3 does not affect the growth rate σ. On the other hand, examining $\det(A - \sigma B) = 0$ shows that changing the sign of k_1 changes the sign of σ. Also, Johnson (1963) established that unstable modes cannot exist for $|k_1| > 1$. Therefore, the stability of the flow field in the domain of $k_1 \in [0, 1]$ and $k_3 \in [0, \infty)$ may be studied without a loss of generality.

3. Evolution of horizontal vorticity fluctuations

The linearized inviscid fluctuating vorticity equations for the given base flow are as follows, where $s_{ij} = \frac{1}{2}\left(u_{i,j} + u_{j,i}\right)$ and $\bar{\mathrm{D}}/\bar{\mathrm{D}}t = \partial/\partial t + \langle u_1 \rangle \partial/\partial x_1$:

$$\frac{\bar{\mathrm{D}}\omega_i'}{\bar{\mathrm{D}}t} = -u_2' \frac{\partial \langle \omega_i \rangle}{\partial x_2}\delta_{i3} + \left(\omega_2'\delta_{i1} + \omega_1'\delta_{i2}\right)\langle s_{12} \rangle + \left(\langle \omega_3 \rangle + 2\Omega\right) s_{i3}' + \epsilon_{ik3}\Omega\omega_k' - Ri_b \epsilon_{ij3}\frac{\partial \rho'}{\partial x_j}. \tag{3.1}$$

The behaviour of the inertial instability in either a strongly stratified or a homogeneous fluid can be explained by looking at the inviscid linearized evolution equations for the horizontal fluctuating vorticity components. They are given below, letting $S(x_2)$ denote local mean shear which takes its maximum non-dimensional value of 1 where $x_2 = 0$, and noting that $\langle \omega_3 \rangle (x_2) = -S(x_2)$:

$$\frac{\bar{\mathrm{D}}\omega_1'}{\bar{\mathrm{D}}t} = \frac{\omega_2'}{2}\left(S(x_2) + 2\Omega\right) + \left(2\Omega - S(x_2)\right) s_{13}' - Ri_b \frac{\partial \rho'}{\partial x_2}, \tag{3.2}$$

$$\frac{\bar{\mathrm{D}}\omega_2'}{\bar{\mathrm{D}}t} = \frac{\omega_1'}{2}\left(S(x_2) - 2\Omega\right) + \left(2\Omega - S(x_2)\right) s_{23}' + Ri_b \frac{\partial \rho'}{\partial x_1}. \tag{3.3}$$

The first term on the right-hand side of both equations (3.2) and (3.3) physically represents the tilting of vorticity fluctuations by the mean strain combined with the 'fictitious' effect of coordinate system rotation on horizontal vorticity components. The second term in both equations represents the tilting of mean flow absolute vorticity by strain fluctuations. The third term represents vorticity generation via baroclinic torque. The right-hand side can also be expressed in a more mathematically convenient form in terms of fluctuating velocity gradients:

$$\frac{\bar{\mathrm{D}}\omega_1'}{\bar{\mathrm{D}}t} = -S(x_2)\frac{\partial u_3'}{\partial x_1} + 2\Omega\frac{\partial u_1'}{\partial x_3} - Ri_b\frac{\partial \rho'}{\partial x_2}, \tag{3.4}$$

$$\frac{\bar{\mathrm{D}}\omega_2'}{\bar{\mathrm{D}}t} = (2\Omega - S(x_2))\frac{\partial u_2'}{\partial x_3} + Ri_b\frac{\partial \rho'}{\partial x_1}. \tag{3.5}$$

For small k_1 (relative to k_3) or nearly streamwise invariant modes we can simplify these equations:

$$\frac{\bar{\mathrm{D}}\omega_1'}{\bar{\mathrm{D}}t} \approx 2\Omega\omega_2' - Ri_b\frac{\partial \rho'}{\partial x_2}, \tag{3.6}$$

$$\frac{\bar{\mathrm{D}}\omega_2'}{\bar{\mathrm{D}}t} \approx -(2\Omega - S(x_2))\omega_1' + Ri_b\frac{\partial \rho'}{\partial x_1}. \tag{3.7}$$

Taking the material derivative of both sides gives

$$\frac{\bar{\mathrm{D}}^2\omega_1'}{\bar{\mathrm{D}}t^2} \approx 2\Omega\frac{\bar{\mathrm{D}}\omega_2'}{\bar{\mathrm{D}}t} - Ri_b\frac{\bar{\mathrm{D}}}{\bar{\mathrm{D}}t}\left[\frac{\partial \rho'}{\partial x_2}\right], \tag{3.8}$$

$$\frac{\bar{\mathrm{D}}^2\omega_2'}{\bar{\mathrm{D}}t^2} \approx -(2\Omega - S(x_2))\frac{\bar{\mathrm{D}}\omega_1'}{\bar{\mathrm{D}}t} + Ri_b\frac{\bar{\mathrm{D}}}{\bar{\mathrm{D}}t}\left[\frac{\partial \rho'}{\partial x_1}\right]. \tag{3.9}$$

Substituting the linearized evolution equations for horizontal density gradient and vorticity we find:

$$\frac{\bar{\mathrm{D}}^2\omega_1'}{\bar{\mathrm{D}}t^2} \approx -2\Omega(2\Omega - S(x_2))\omega_1' + Ri_b(2\Omega + S(x_2))\frac{\partial \rho'}{\partial x_1} - Ri_b\frac{\partial u_3'}{\partial x_2}, \tag{3.10}$$

$$\frac{\bar{\mathrm{D}}^2\omega_2'}{\bar{\mathrm{D}}t^2} \approx -2\Omega(2\Omega - S(x_2))\omega_2' + Ri_b(2\Omega - S(x_2))\frac{\partial \rho'}{\partial x_2} + Ri_b\frac{\partial u_3'}{\partial x_1}. \tag{3.11}$$

The first terms on the right-hand sides of (3.10) and (3.11) represent the inertial instability and give its maximal growth rate $\sigma = [-2\Omega(2\Omega - S)]^{1/2}$ in the case of constant S. The remaining terms correspond to buoyancy effects. In particular, the second terms represent the shearing and rotation of vorticity induced by density gradients, and the third term represents the influence of isopycnal deformation.

4. Effect of stratification on growth rates

The following analysis is inviscid. The effects of viscosity and diffusion are included for reference in appendices A and B. Growth rates for a strongly stratified non-rotating shear layer are shown in figure 2(*b*) and agree well with figure 3(*b*) of Deloncle *et al.* (2007) and their result that $Ri_b^{-1/2}k_3 = Fr_h k_3$ is the appropriate self-similar vertical scaling. If scaling is not performed then stability plots grow vertically with a wavenumber band proportional to N. The growth rates for the homogenous case are included in figure 2(*a*) for comparison. Weakly stratified cases, where $Ri_b < O(1)$,

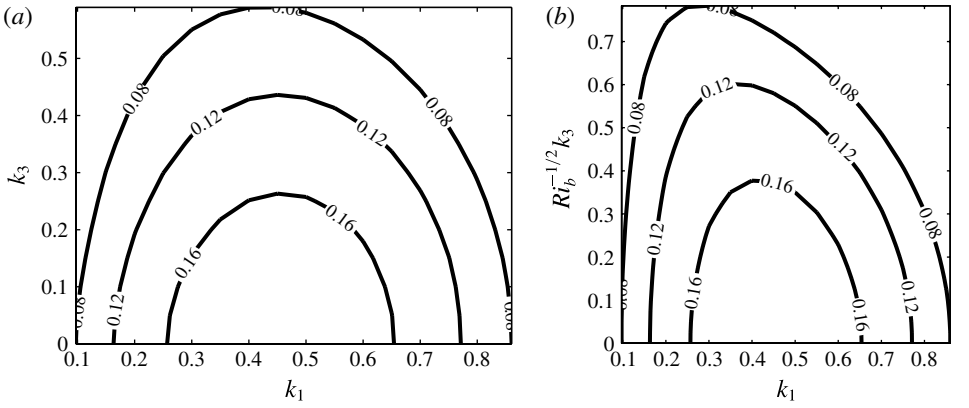

FIGURE 2. Plots of growth rate for (*a*) the inviscid non-rotating homogeneous case and (*b*) the non-rotating strongly stratified case where $Ri_b = 4$. The maximum growth rates are observed when $k_3 = 0$ and $k_1 = 0.44$ with a growth rate of $\sigma = 0.190$ as in Deloncle *et al.* (2007).

are found to be qualitatively similar to the unstratified cases as in Deloncle *et al.* (2007) and will not be discussed.

4.1. *Moderate rotation regime*

Plots (*b,c*) from figure 3 show the effect of stratification on growth rates when $2\Omega = 0.1$. Plots (*e,f*) show the same for $2\Omega = 0.9$, and plots (*h,i*) for $2\Omega = 1$. These plots suggest that for $Ri_b \gtrsim 1$, self-similarity of the form $\sigma\,(k_1, k_3, Ri_b, 2\Omega) = \sigma\left(k_1, Ri_b^{-1/2}k_3, 2\Omega\right)$ is observed. This result is consistent with the analysis of Billant & Chomaz (2001), which states that self-similarity of strongly stratified flows holds in a rotating coordinate system. Similar collapse when $Ri_b > 1$ was observed at all other values of 2Ω explored in this analysis.

In figure 3(*a–c*), the inertial instability corresponds to the growth rates near the k_3 axis, but away from the k_1 axis. In the limit of $k_3 \to \infty$, growth rates for $2\Omega = 0.1$ approach the maximal inertial growth rate of $\sqrt{-2\Omega\,(2\Omega - S_{max})} = 0.3$ where S_{max} is the maximal shear which takes the non-dimensional value of unity. Stratification reduces the intensity of growth rates associated with the inertial instability for moderate values of $Ri_b^{-1/2}k_3$. In the limit of $k_3 \to \infty$, the cases with and without stratification are equivalent, but this limit is not realized until very large values of $Ri_b^{-1/2}k_3$, where the influence of stratification becomes negligible. Figure 3(*d–f*) show growth rates for unstratified, $Ri_b = 1$ and $Ri_b = 10$ cases, respectively, with stronger anticyclonic rotation ($2\Omega = 0.9$). In the unstratified case there are distinct regions corresponding to the inertial and barotropic instabilities. In the stratified cases this distinction is far less apparent, with growth rates showing little variation with respect to $Ri_b^{-1/2}k_3$.

Stratification leads to a strong qualitative change in the zero absolute vorticity case ($2\Omega = 1$), a key result of this paper. We define the zero absolute vorticity case as the case where absolute vorticity is zero at the inflection point. Figure 3(*g–i*) show the growth rates associated with unstratified, $Ri_b = 1$ and $Ri_b = 10$ cases, respectively, for $2\Omega = 1$. The inertial instability disappears when $2\Omega = 1$. Even though the inertial

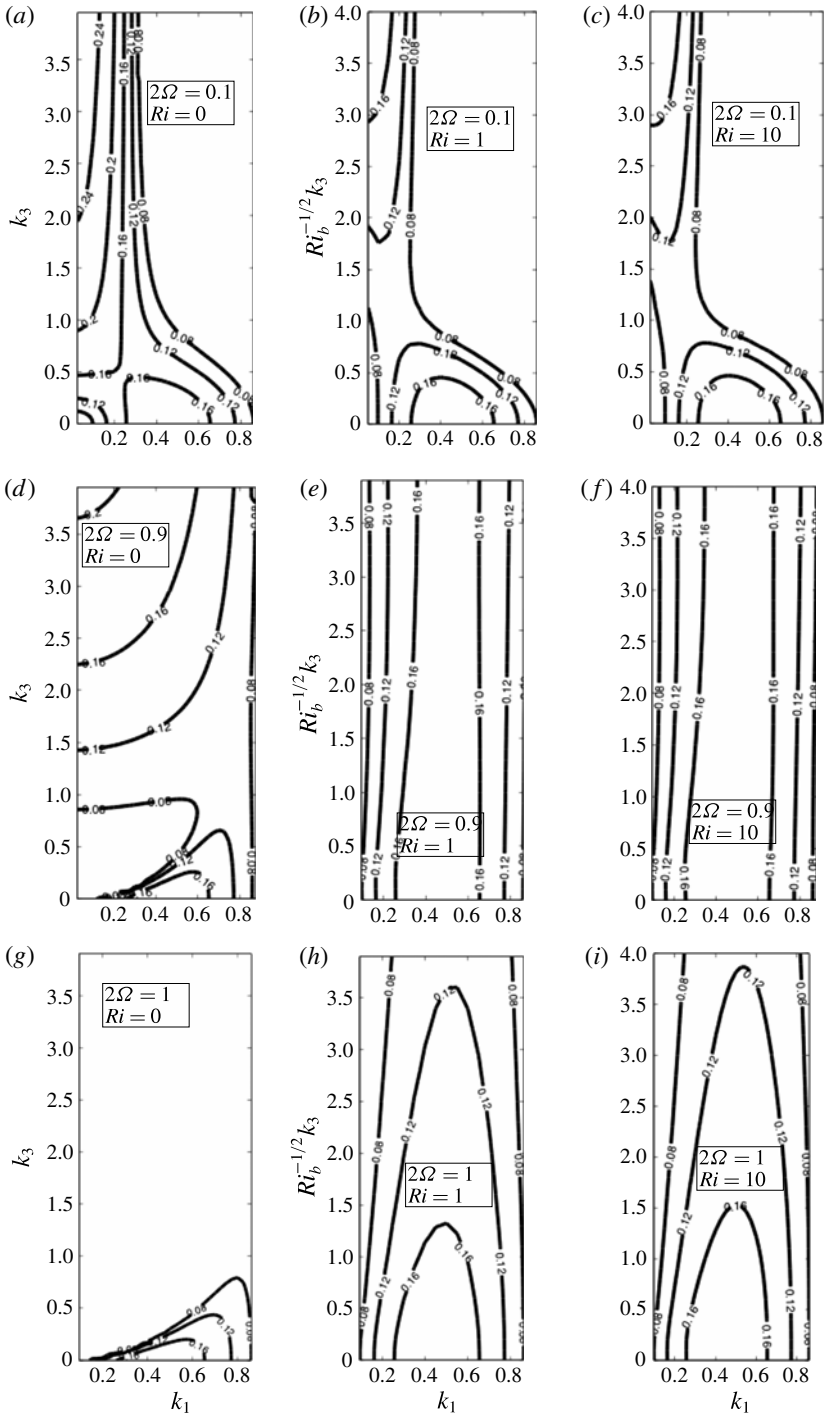

FIGURE 3. Contour plots of growth rate, with the three columns (left to right) corresponding to $Ri_b = 0$, 1 and 10, respectively, and the three rows (top to bottom) corresponding to $2\Omega = 0.1$, 0.9 and 1, respectively.

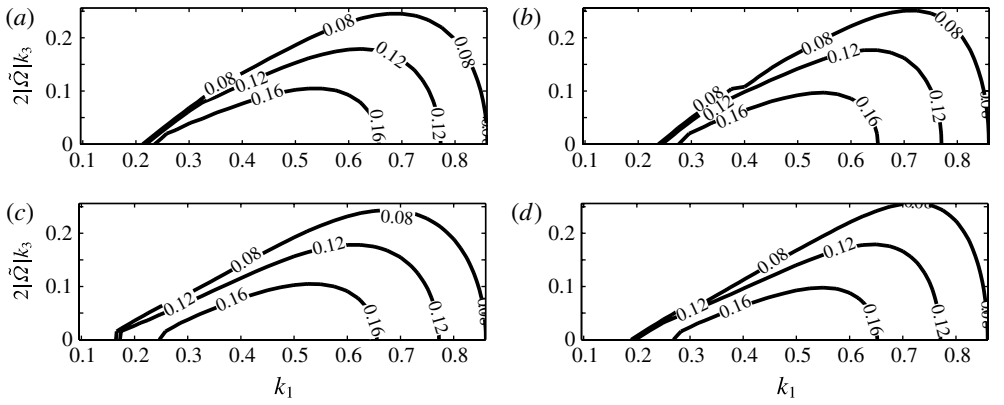

FIGURE 4. Contour plots of growth rate in the regime of rapid rotation for unstratified flow: (*a*) the $2\Omega = -4$ case, (*b*) the $2\Omega = 5$ case, (*c*) the $2\Omega = -2$ case and (*d*) the $2\Omega = 3$ case.

instability is suppressed, a far greater range of vertical wavenumbers is unstable than when there is no rotation for strongly stratified flow. Comparison of $\sigma = 0.12$ contours from figures 2(*b*) and 3(*i*) shows a much wider range of $Ri_b^{-1/2}k_3$ values associated with this growth rate for the zero absolute vorticity case. Some modes remain unstable even when $Ri_b^{-1/2}k_3 \approx 20$ (not shown in the figure).

Looking at figure 3(*a–i*) we see that increasing anticyclonic rotation rates toward the zero absolute vorticity state increases the range of k_1 values associated with inertial instability for both unstratified and strongly stratified cases. In the strongly stratified cases, near the zero absolute vorticity state, the barotropic instability is greatly modified. The distinction between growth rates associated with inertial and barotropic modes is much less apparent for strongly stratified flow.

4.2. *Rapid rotation regime*

Plots (*a–d*) in figure 4 show growth rates for various rapid rotation rates. Figure 4(*a,b*) show well-collapsed growth rates with respect to vertical scale $2|\tilde{\Omega}|k_3 = 2|(\Omega - 1/4)|k_3$ when rotation rates are $2\Omega = -4$ and $2\Omega = 5$ respectively. While slight differences are seen in figure 4(*c,d*) at slower rotation rates, collapse is still reasonably good. Scaling was found to be better when vertical wavenumbers were scaled using $2|\tilde{\Omega}|$ instead of $2|\Omega|$. This scaling is the difference in angular velocity with respect to $\Omega = 1/4$, which is the most destabilizing rotation rate as seen in (3.10) and (3.11) for $S = 1$. Plots (*a–d*) in figure 5 show similar collapse for strongly stratified flow. However, the numerical values of rotation rate required for such collapse are higher when the stratification is large. It is worth noting the associated vertical scale is $2|\tilde{\Omega}|Ri_b^{-1/2}k_3 \sim (f/N)\,k_3$, which agrees with the results of Smyth & McWilliams (1998) when $\tilde{\Omega}$ is large. Some asymmetry with respect to the sign of $\tilde{\Omega}$ is observed for the cyclonic case (*c*) and anticyclonic case (*d*) from figure 5. As the rapidly rotating regime is approached, the anticyclonic case has a wider range of unstable vertical wavenumbers than the cyclonic case with equivalent $|\tilde{\Omega}|$. As in Smyth & McWilliams (1998), we find that rotation rates do not have to be very rapid to be well-approximated by the rapidly rotating strongly stratified regime. Rapid rotation

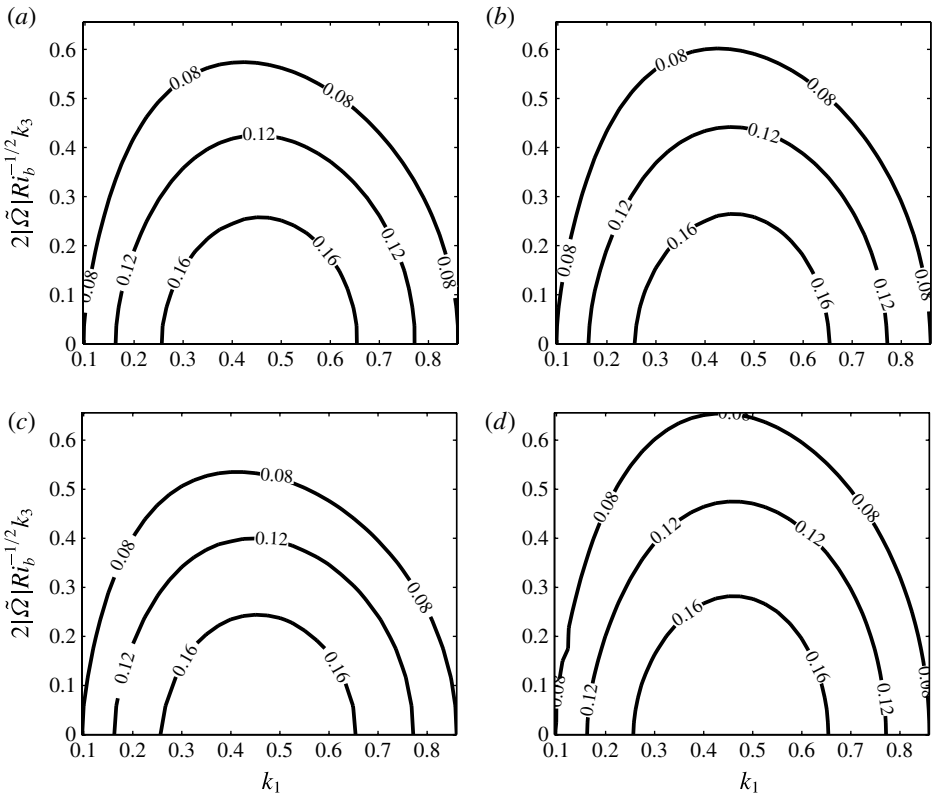

FIGURE 5. Contour plots of growth rate in a strongly stratified case ($Ri_b = 10$) in the rapidly rotating regime. Shown for (*a*) the $2\Omega = -14$ case, (*b*) the $2\Omega = 15$ case, (*c*) the $2\Omega = -3$ case and (*d*) the $2\Omega = 4$ case.

leads to (3.10) and (3.11) taking the following form for small k_1 modes:

$$\frac{\bar{\mathrm{D}}^2\omega_1'}{\bar{\mathrm{D}}t^2} \approx -4\Omega^2\omega_1' + Ri_b 2\Omega \frac{\partial \rho'}{\partial x_1} - Ri_b \frac{\partial u_3'}{\partial x_2}, \tag{4.1}$$

$$\frac{\bar{\mathrm{D}}^2\omega_2'}{\bar{\mathrm{D}}t^2} \approx -4\Omega^2\omega_2' + Ri_b 2\Omega \frac{\partial \rho'}{\partial x_2} + Ri_b \frac{\partial u_3'}{\partial x_1}. \tag{4.2}$$

Equations (4.1) and (4.2) imply that when stratification is negligible, horizontal vorticity is attenuated and, correspondingly, figure 4 shows that strong stabilization is observed for modes with $k_1 \lesssim 2|\tilde{\Omega}|k_3$ for a rapidly rotating homogeneous fluid. No such effect is observed in the presence of strong stratification as seen in figure 5 implying that the second and/or third terms in (4.1) and (4.2) offset the strongly stabilizing effect of the first term.

5. Eigenmodes

Figure 6 shows new variables n, s and θ and their relationship to the physical coordinate system presented in figure 1. These variables simplify visualization of eigenmodes. Introducing characteristic variable $Ks = k_1x_1 + k_3x_3$ allows solutions to be represented in two-dimensional form where a flow variable ϕ has the functional

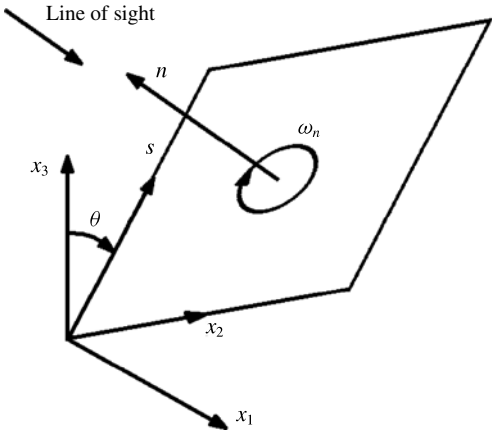

FIGURE 6. The phase variable s, measuring distance along the $\boldsymbol{k}$-axis. Planes are displayed in a manner such that the normal vector has a positive vertical component so that visualization is more straightforward.

form $\phi(x_2, s) = \mathrm{Re}\left[\phi(x_2)\exp(\mathrm{i}Ks)\right]$. Solutions are wavelike with wavenumber $K = \sqrt{k_1^2 + k_3^2}$ and oriented with an angle $\theta = \tan^{-1}(k_1/k_3)$ between the x_3 direction and the wavenumber vector, $\boldsymbol{k} = k_1\boldsymbol{e}_1 + k_3\boldsymbol{e}_3$, where $\boldsymbol{e}_1$ and $\boldsymbol{e}_3$ are unit vectors in x_1 and x_3 directions, respectively. Because k_1 and k_3 are non-negative, increasing s corresponds to increasing x_1 and/or x_3. The vector normal to the wavenumber vector in the x_1–x_3 plane is denoted by $\boldsymbol{n}$. Two new flow variables, normal vorticity fluctuations, $\omega_n' = \omega_i' n_i = -\omega_1' \cos\theta + \omega_3' \sin\theta$, and normal velocity fluctuations, $u_n' = u_i' n_i = -u_1' \cos\theta + u_3' \sin\theta$, are introduced to visualize unstable modes in the new coordinates. For inertial modes, k_1 is small in comparison to k_3, meaning $\boldsymbol{n} \sim -\boldsymbol{e}_1$ and $\boldsymbol{k} \sim \boldsymbol{e}_3$.

The base state contains no available potential energy, therefore the overall effect of buoyancy on vertical fluctuations is stabilizing. However, certain physical mechanisms, one example is the zigzag instability of Billant & Chomaz (2000), can result in faster growing modes than possible in an unstratified fluid. It is worth noting that $u_3' = u_s' \cos\theta + u_n' \sin\theta$ so that, for an inclination θ, the normal velocity u_n' leads to vertical motion. Even if ρ' has the same sign as u_3', implying that the buoyancy term in the vertical momentum equation has a stabilizing effect on vertical fluctuations, ρ' can have a different sign than u_s' or u_n'. Thus, buoyancy may have a stabilizing effect on u_s' and destabilizing effect on u_n' or vice versa, while still stabilizing vertical motion.

5.1. *Strongly stratified non-rotating regime*

Figure 7 shows the form of barotropic modes with non-zero k_3 for a non-rotating strongly stratified case. Figure 7(*c*) shows quasi-streamwise parcels of buoyant fluid with large lateral spread. Density fluctuations in these parcels are maintained by vertical fluctuations due to jets of u_n' in the shear region as seen in figure 7(*b*). It is apparent that u_n' and ρ' are of the same sign so that the effect of stratification is stabilizing on u_n' fluctuations. Figure 7(*a,d*) show an array of alternating jets that are oriented in the lateral direction (x_2) outside of the shear region, but inclined with respect to the vertical and streamwise directions within the shear region. The physics driving this instability can be illustrated through the following arguments. A flow field

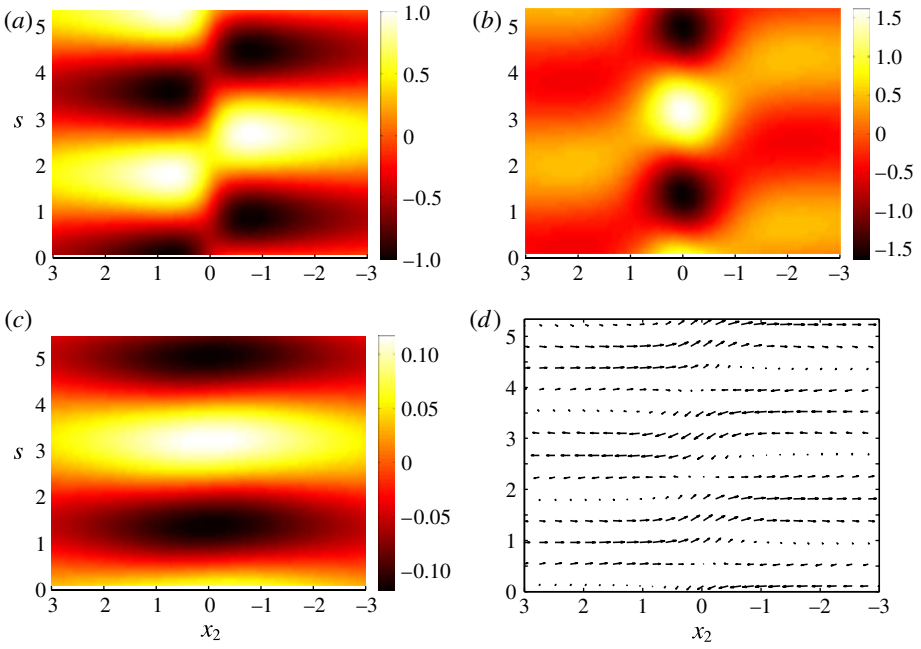

FIGURE 7. (Colour online available at journals.cambridge.org/flm) Plots of (*a*) ω_n', (*b*) u_n', (*c*) ρ' and (*d*) velocity vectors for a barotropic mode from a non-rotating case with strong stratification, $Ri_b = 10$, $2\Omega = 0$, $k_1 = 0.3$, $k_3 = 1.7$ and $\theta = 10.0°$.

begins with alternating layers of heavy and light fluid on top of one another that are not infinite, but spread far beyond the shear region as observed in figure 7(*c*). Lateral variation in density within the layers of buoyant fluid results in currents with u_2' directed towards and away from the shear region as seen in figure 7(*d*). Heavy parcels approach the shear region with slight negative vertical velocity, while light parcels approach the shear region with slight positive vertical velocity. As the currents induced by ω_n' enter the shear region they encounter buoyant quasi-streamwise currents increasing their density anomaly, resulting in larger vertical velocity magnitudes until exiting the shear region on the opposite side of the buoyant layer. These quasi-lateral currents induce vertical shear $\left(\partial u_2'/\partial x_3 \sim \partial u_2'/\partial s\right)$, as seen in figure 7(*d*), which then acts to generate ω_2' through tilting of mean vertical vorticity. Tilting of the ω_1' contained in the currents by the mean shear also leads to ω_2' formation. The resulting ω_2' coincides with the quasi-streamwise jets observed in figure 7(*b*).

The density structures observed in figure 7 are reminiscent of density intrusions observed in the experiments of Ivey & Corcos (1982), Thorpe (1982), Browand, Guyomar & Yoon (1987) and Liu, Maxworthy & Spedding (1987) and the numerical simulations of Basak & Sarkar (2006). The mechanism proposed in these works involves vertical mixing that leads to tongues of downward-propagating heavier fluid encountering tongues of upward-propagating lighter fluid and then spreading laterally similarly to gravity currents. The arguments provided in the previous paragraph referring to the eigenmode described in figure 7 offer an illustration of a linear mechanism that generates layers of buoyant fluid. These density structures could lead to a periodic array of non-turbulent density intrusions outside of the shear region where vertical mean vorticity is negligible.

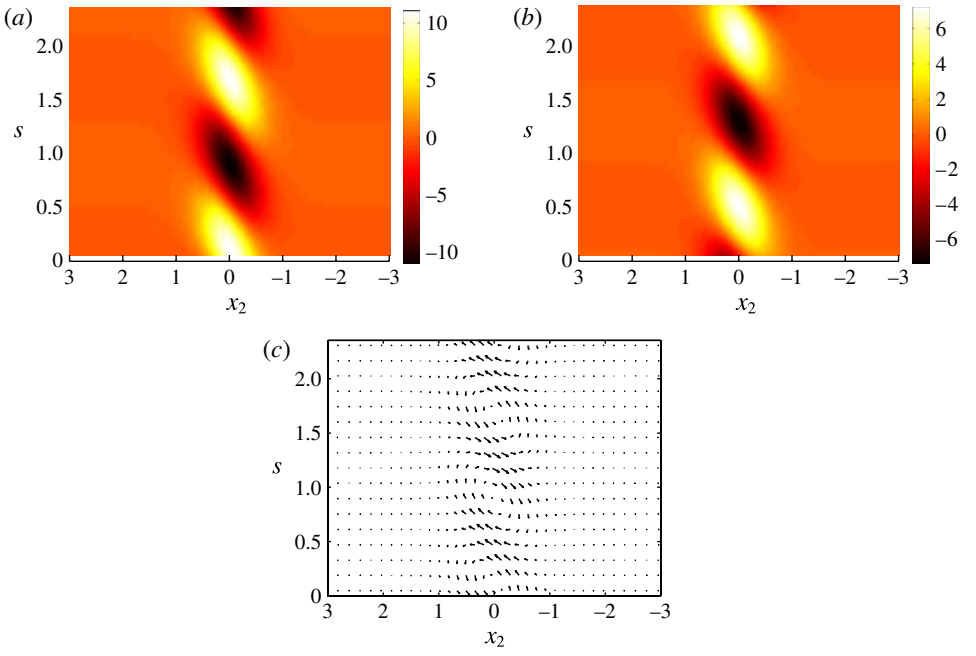

FIGURE 8. (Colour online) Plots of (*a*) ω_n', (*b*) u_n' and (*c*) velocity vectors for an inertial mode in a weak anticyclonic case without stratification, $Ri_b = 0$, $2\Omega = 0.1$, $k_1 = 0.1$, $k_3 = 4$ and $\theta = 1.43°$.

5.2. *Moderate rotation regime*

Figure 8 shows an inertial mode in a homogeneous fluid with fairly weak anticyclonic rotation ($2\Omega = 0.1$). Since $\theta = 1.43°$ the plane is quasi-vertical, therefore we can make the approximations $\omega_n' \sim -\omega_1'$ and $\partial u_n'/\partial s \sim -\omega_2'$ to infer horizontal vorticity fluctuations from figure 8(*a*,*b*). Parcels of fluid with like-signed ω_1' and ω_2' occupy the region where $|x_2| < 0.5$. For $0 < 2\Omega < S\,(x_2)$, the condition of inertial instability, (3.6) and (3.7) show that ω_1' and ω_2' must have the same sign for growth of the instability, otherwise mean shear cannot intensify horizontal vorticity fluctuations via vortex stretching. Figure 8(*c*) shows velocity vectors corresponding to the ω_n' field from 8(*a*) to aid in visualization. It is clear that positive (negative) ω_n' corresponds to counterclockwise (clockwise) rotation in the $(-x_2, s)$ plane. In later figures, velocity vectors are included for eigenmodes when it is more difficult to infer velocities from ω_n' plots.

Figure 9 shows an inertial mode with the same anticyclonic rotation rate but in a strongly stratified fluid. The lateral spread of vorticity fluctuations has increased considerably for inertial modes in a strongly stratified fluid compared to the homogeneous case in figure 8. Looking at the region of positive ω_n' from figure 9(*a*) and corresponding density fluctuations from figure 9(*c*) it is clear that the vertical motion induced by ω_n' has the same sign as the density field such that buoyancy stabilizes ω_n' fluctuations. The normal component of the baroclinic term of (3.1) is shown in figure 9(*d*), further illustrating the stabilizing effect of buoyancy on ω_n'. Similarly, looking at regions of positive u_n' from figure 9(*b*) and corresponding density fluctuations from figure 9(*c*) the stabilizing effect of buoyancy on u_n' can be deduced. Density fluctuations are generated by both ω_n' and u_n' implying that buoyancy plays a

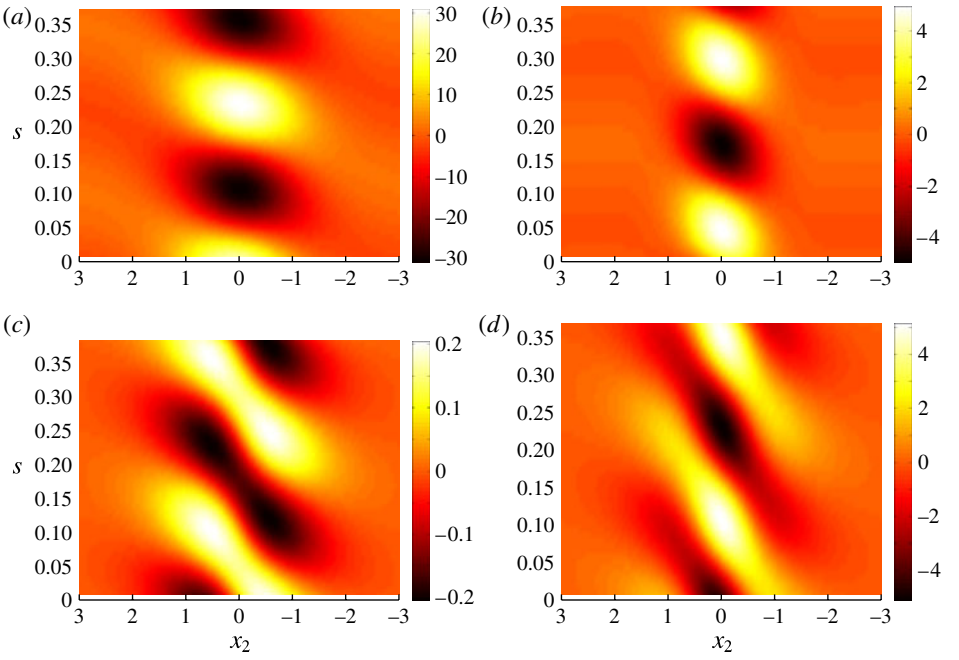

FIGURE 9. (Colour online) Plots of (*a*) ω_n', (*b*) u_n', (*c*) ρ' and (*d*) the normal component of the baroclinic term from (3.1) for an inertial mode in a weak anticyclonic case with stratification, $Ri_b = 10$, $2\Omega = 0.1$, $k_1 = 0.1$, $k_3 = 25.3$ and $\theta = 0.23°$.

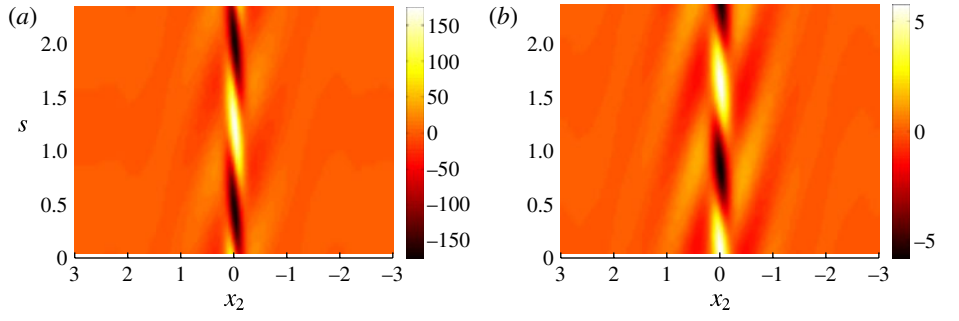

FIGURE 10. (Colour online) Plots of (*a*) ω_n' and (*b*) u_n' for a near-zero absolute vorticity case without stratification, $Ri_b = 0$, $2\Omega = 0.95$, $k_1 = 0.444$, $k_3 = 4$ and $\theta = 6.33°$.

stabilizing role, inhibiting generation of horizontal vorticity fluctuations via baroclinic torque.

Figure 10 shows an inertial mode in a homogeneous fluid with nearly zero absolute mean vorticity at the inflection point ($2\Omega = 0.95$). As with the weak anticyclonic cases presented in figures 8 and 9, we observe regions of like-signed ω_1' and ω_2'. The lateral spread of the vorticity fluctuations is small because the local value of $-2\Omega\,(2\Omega - S\,(x_2))$ has positive values only at $x_2 \sim 0$ where $S > 2\Omega > 0$. The small lateral spread of the unstable region leads to a large angle of inclination for ω_n' structures with respect to the x_2 direction as compared with the weaker anticyclonic

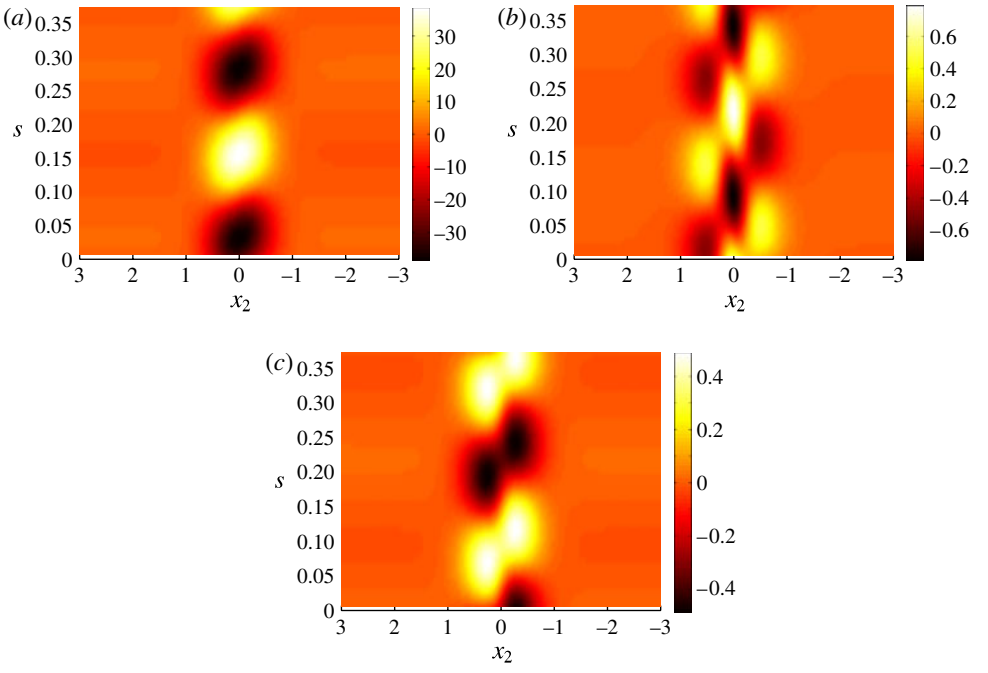

FIGURE 11. (Colour online) Plots of (*a*) ω_n', (*b*) u_n' and (*c*) ρ' for a barotropic mode from a zero absolute vorticity case with stratification, $Ri_b = 10$, $2\Omega = 1$, $k_1 = 0.444$, $k_3 = 25.3$ and $\theta = 1.0°$.

case in figure 8(*a*). Figure 11 shows a large k_3 mode from the strongly stratified case with zero absolute mean vorticity at the inflection point. A dramatic difference in dynamics is observed between this mode and the inertial mode from figure 10. Density fluctuations are generated by ω_n', but the u_n' field in figure 11(*b*) has the opposite sign to the ρ' field in figure 11(*c*). Therefore, u_n' fluctuations are aligned with the buoyancy force rather than opposed to it for the inertial mode in figure 9. This destabilizing effect of buoyancy on u_n' is in contrast to the stabilizing effect seen earlier in the weak anticyclonic case. When $2\Omega = S$, the linearized fluctuating vorticity equations take the following form at the inflection point where $\langle u_1 \rangle = 0$,

$$\frac{\partial \omega_1'}{\partial t} = \left(\frac{S}{2} + \Omega\right)\omega_2' - Ri_b \frac{\partial \rho'}{\partial x_2}, \tag{5.1}$$

$$\frac{\partial \omega_2'}{\partial t} = Ri_b \frac{\partial \rho'}{\partial x_1}. \tag{5.2}$$

Thus, for this base state, unstratified flow with zero absolute vorticity contains no mechanism to generate ω_2', which is why the zero absolute vorticity state tends to stabilize barotropic modes in homogeneous fluids as noted in § 4.

The buoyancy-driven instability in the case of zero absolute vorticity can be explained as follows. Quasi-streamwise vortices indicated by ω_n' in figure 11(*a*) distort isopycnals such that positively buoyant fluid is on one side of the vortices and negatively buoyant fluid is on the other, as observed in figure 11(*c*). The slight inclination of the quasi-streamwise vortices in the vertical direction, due to the small vertical component of $\boldsymbol{n}$, leads to the associated density gradient having

a slight streamwise component $\partial\rho'/\partial x_1$ which in turn leads to baroclinic formation of lateral vorticity, ω_2', according to (5.2). The formation of ω_2' is reflected by the velocity gradient, $\partial u_n'/\partial s \sim -\partial u_1'/\partial x_3$, seen in figure 11(*b*). The lateral vorticity, ω_2', is then transferred to the quasi-streamwise vorticity, $\omega_1' \sim -\omega_n'$, via coordinate system rotation and strain-induced tilting, according to (5.1), closing the creation cycle for this disturbance. An important point is that without a slight vertical component in $\boldsymbol{n}$, there is no mechanism to generate ω_2' fluctuations.

The contours for eigenmodes in figures 8–11 show a change in inclination angle with respect to the x_2 direction from positive to negative as rotation rate increases. The sign change occurs near the zero absolute vorticity state. This phenomenon can be explained through analysis of the buoyancy-driven instability present when absolute vorticity is nearly zero. Equation (5.2) implies that, in order for modes to grow in the zero absolute vorticity state, baroclinic torque must generate ω_2' fluctuations. More precisely, the product of ω_2' and (5.2) implies that $\partial\rho'/\partial x_1$ must have the same sign as ω_2' for growth of $\omega_2'\omega_2'$. Because the base state has no baroclinicity, there is no net enstrophy production and baroclinic torque therefore inhibits ω_1' fluctuations, i.e. the product of ω_1' and (5.1) implies that $\partial\rho'/\partial x_2$ must have the same sign as ω_1' for suppression of $\omega_1'\omega_1'$. Owing to the small tilt of $\boldsymbol{k}$ in the positive streamwise direction (x_1), $\partial\rho'/\partial x_1$ and $\partial\rho'/\partial x_3$ have the same sign. In order for ω_1' fluctuations to grow, ω_1' and ω_2' must have the same sign, since the first term on the right-hand side of (5.1) must be a source. Thus, isocontours of ρ' in the x_2–x_3 plane should have a negative angle ($\partial\rho'/\partial x_2$ and $\partial\rho'/\partial x_3$ of the same sign) as observed in figure 11. Similar analysis of the weak anticyclonic case yields a positive angle.

5.3. *Rapid rotation regime*

Figure 12 shows modes from a rapidly rotating and strongly stratified case. Thermal wind balance explains many of the differences between this case and the non-rotating strongly stratified modes seen in figure 7 with horizontal density variations correlating appropriately with the observed vertical shear. From figure 12(*b,d*) we observe that regions of positive (negative) u_n' correlate with regions of negative (positive) u_s' implying that associated regions contain negative (positive) u_1'. By examining figure 12(*b–d*), the signs of both $\partial u_1'/\partial x_3$ and $\partial\rho'/\partial x_2$ can be determined near the inflection point. Positive values of $\partial u_1'/\partial x_3$ are found to correlate with negative values of $\partial\rho'/\partial x_2$ and vice versa as expected from thermal wind balance.

6. Conclusions

The three-dimensional instability of a stratified and rotating horizontally oriented hyperbolic shear layer has been investigated. For weak to moderate rotation rates, stratification was found to stabilize the inertial instability. The distinction between growth rates associated with inertial and barotropic modes lessened for strongly stratified flow as the zero absolute vorticity state was approached. For strongly stratified flow with zero absolute vorticity at the inflection point, the vertical wavenumber band associated with barotropic instability significantly widened in comparison to the non-rotating case.

Rapid rotation and/or strong stratification was found to result in self-similarity of growth rates when the vertical wavenumber of perturbations was scaled appropriately. For unstratified rapidly rotating cases, such self-similarity was found when vertical wavenumbers were scaled as $2|\tilde{\Omega}|k_3/S$ where $2\tilde{\Omega} = 2\,(\Omega - 1/4)$ corresponds to the deviation with respect to the most destabilizing rotation rate. While the difference

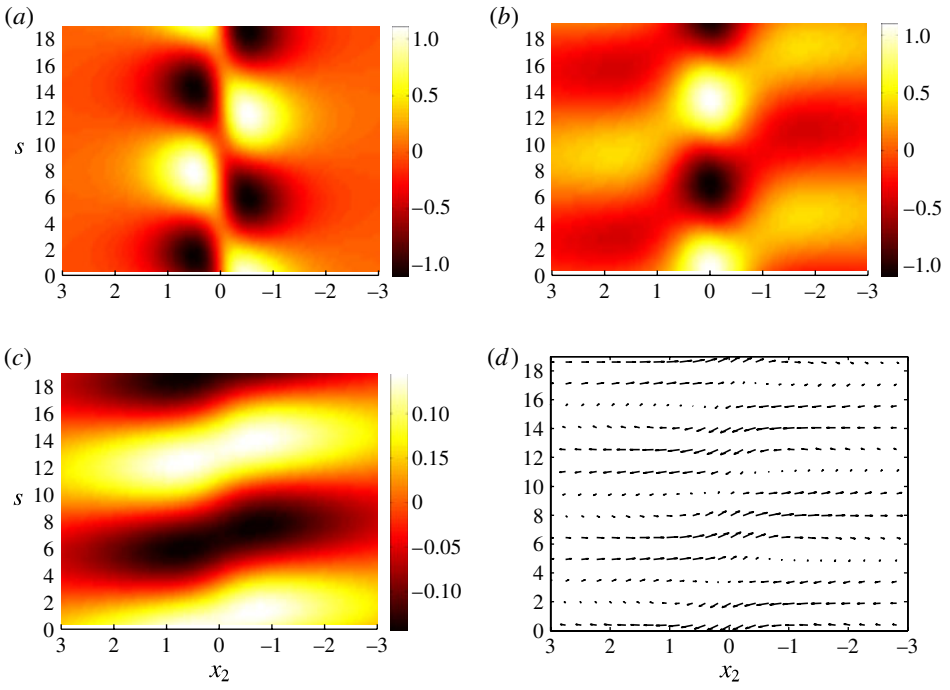

FIGURE 12. (Colour online) Plots of (*a*) ω_n', (*b*) u_n', (*c*) ρ' and (*d*) velocity vectors for a barotropic mode from a rapidly rotating case with strong stratification, $Ri_b = 10$, $2\Omega = -2$, $k_1 = 0.3$, $k_3 = 0.4$ and $\theta = 36.9°$.

between Ω and $\tilde{\Omega}$ is not significant in geostrophic flows, the difference is appreciable for less rapidly rotating cases such as submesoscale shear flows where $2|\Omega|/S$ is not particularly large. This scaling is consistent with the Taylor–Proudman theorem in the limit of $|\Omega| \to \infty$, where only $k_3 = 0$ modes are unstable. For strongly stratified rapidly rotating cases, self-similarity of growth rates required vertical wavenumbers to scale as $2|\tilde{\Omega}|k_3/N$. This result is consistent with quasi-geostrophy for very large $2|\Omega|/S$ and N/S, but the distinction between Ω and $\tilde{\Omega}$ is still non-negligible in the submesoscale regime. Rapid rotation was also found to stabilize low k_1, high k_3 modes in an unstratified fluid. Such stabilization is not observed in the presence of strong stratification.

Analysis of eigenmodes provided insight regarding the underlying physics of the inertial instability and barotropic instability in a rotating strongly stratified fluid for small amplitude perturbations. Analysis of a non-rotating strongly stratified barotropic mode showed a potential linear mechanism for generation of density intrusions. For weakly anticyclonic flow, quasi-streamwise vortices associated with the inertial instability were suppressed via baroclinic torque when stratification was strong. For the strongly stratified zero absolute vorticity case, density anomalies generated by quasi-streamwise vortices with a small vertical inclination led to baroclinic formation of lateral vorticity which, through tilting by system rotation and strain, sustains the quasi-streamwise vortices. This mechanism is fundamentally different than the mechanism driving barotropic modes when only rotation or stratification effects are included. Rapid rotation was found to modify the strongly stratified barotropic mode in a manner consistent with thermal wind balance.

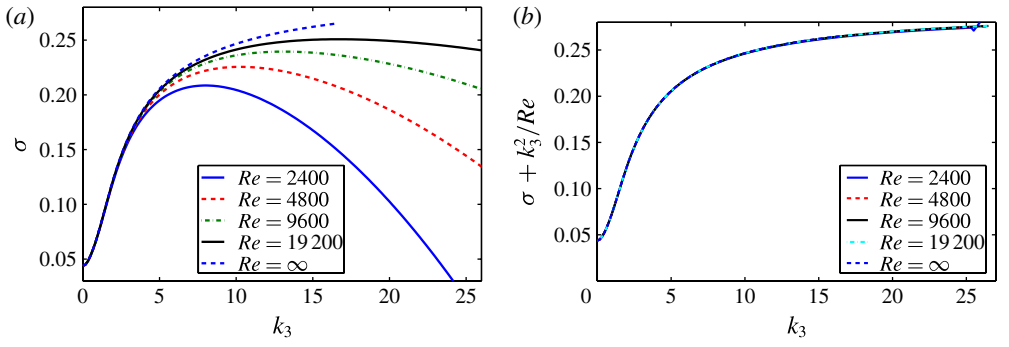

FIGURE 13. (Colour online) Effect of Re on (a) growth rates associated with inertial instability and (b) collapsed growth rates based on (A 1) where $Ri_b = 1$, $2\Omega = 0.1$, $Pr = 1$ and $k_1 = 0.05$.

In a follow-up paper the nonlinear evolution of the stratified and rotating horizontal shear layer will be explored using direct numerical simulation and comparisons will be made between linear and nonlinear physics.

Acknowledgements

The authors are pleased to acknowledge support by the Jacobs School Graduate Fellowship for E.A. and the National Science Foundation CDI program through Grant No. OCE-0835839 for S.S. and E.A. The authors also are grateful for computational resources through the Triton Affiliations and Partners Program at San Diego Supercomputing Center. Discussions with J. R. Taylor contributed greatly to the scope of this work.

Appendix A. Effect of viscosity

The effects of Re are important to consider, because viscosity sets the vertical length scale at which the inertial instability occurs. For inviscid flows, the inertial instability tends to its maximal growth rate in the limit of $k_3 \to \infty$. The effect of viscosity on the inertial instability for large Re is rather straight-forward as seen in figure 13, with the viscous growth rates being well-approximated by the following relation when the right-hand side is non-negative,

$$\sigma\,(k_1, k_3, Ri_b, 2\Omega, Re) \approx \sigma\,(k_1, k_3, Ri_b, 2\Omega, Re = \infty) - \frac{k_3^2}{Re}. \tag{A 1}$$

This relation can be obtained from substitution of (2.14) into the linearized momentum equations in (2.11) and assuming large vertical gradients. For moderate Re, the effect of viscosity for moderate k_3 values is non-negligible and the horizontal terms of the Laplacian are relevant. In the context of high Re flows, viscosity appears to simply attenuate high k_3 modes with growth rates given by (A 1).

Appendix B. Effect of diffusion

The effects of modifying Pr on both the inertial and barotropic instabilities are shown in figure 14. Low Pr (high mass diffusion) flows behave more like unstratified flows at small scales (large k_3), with smoother density profiles, consistent with the

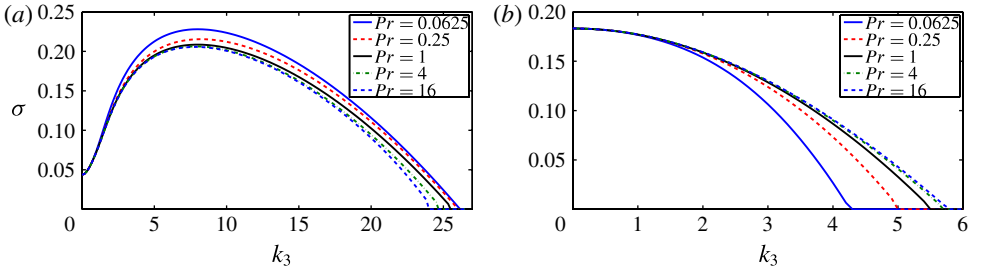

FIGURE 14. (Colour online) Effect of Pr on growth rates associated with (a) the inertial instability and (b) the barotropic instability, where (a) $Re = 2400$, $Ri_b = 1$, $2\Omega = 0.1$ and $k_1 = 0.05$ and (b) $Re = 250$, $Ri_b = 100$, $2\Omega = 0$ and $k_1 = 0.444$.

results presented in figure 14. The inertial instability is destabilized as mass diffusion increases (Pr decreases) as seen in figure 14(a). The barotropic stability, on the other hand, is stabilized as mass diffusion increases as seen in figure 14(b). This is due to the fact that stratification tends to stabilize the inertial instability, but strong stratification is responsible for reducing the selectivity of shear instability in stratified flows.

REFERENCES

BASAK, S. & SARKAR, S. 2006 Dynamics of a stratified shear layer with horizontal shear. *J. Fluid Mech.* **568**, 19–54.

BILLANT, P. & CHOMAZ, J. M. 2001 Self-similarity of strongly stratified inviscid flows. *Phys. Fluids* **13** (6), 1645–1651.

BILLANT, P. & CHOMAZ, J.-M. 2000 Experimental evidence for a new instability of a vertical columnar vortex pair in a strongly stratified fluid. *J. Fluid Mech.* **418**, 167–188.

BROWAND, F. K., GUYOMAR, D. & YOON, S.-C. 1987 The behaviour of a turbulent front in a stratified fluid: experiments with an oscillating grid. *J. Geophys. Res.* **92** (C5), 5329–5341.

DELONCLE, A., BILLANT, P. & CHOMAZ, J.-M. 2011 Three-dimensional stability of vortex arrays in a stratified and rotating fluid. *J. Fluid Mech.* **678**, 482–510.

DELONCLE, A., CHOMAZ, J. & BILLANT, P. 2007 Three-dimensional stability of a horizontally sheared flow in a stably stratified fluid. *J. Fluid Mech.* **570**, 297–305.

DUNKERTON, T. J. 1981 On the inertial stability of the equatorial middle atmosphere. *J. Atmos. Sci.* **38**, 2354–2365.

GRIFFITHS, S. D. 2003 Nonlinear vertical scale selection in equatorial inertial instability. *J. Atmos. Sci.* **60**, 977–990.

HOLTON, J. R. 1992 *An Introduction to Dynamic Meteorology*. Academic.

IVEY, G. N. & CORCOS, G. M. 1982 Boundary mixing in a stratified fluid. *J. Fluid Mech.* **121**, 1–26.

JOHNSON, J. A. 1963 The stability of shearing motion in a rotating fluid. *J. Fluid Mech.* **17**, 337–352.

KLOOSTERZIEL, R. C. & CARNEVALE, G. F. 2008 Vertical scale selection in inertial instability. *J. Fluid Mech.* **594**, 249–269.

KLOOSTERZIEL, R. C., ORLANDI, P. & CARNEVALE, G. F. 2007 Saturation of inertial instability in rotating planar shear flows. *J. Fluid Mech.* **583**, 413–422.

LIU, Y. N., MAXWORTHY, T. & SPEDDING, G. R. 1987 Collapse of a turbulent front in a stratified fluid 1. Nominally two-dimensional evolution in a narrow tank. *J. Geophys. Res.* **92** (C5), 5427–5433.

PLOUGONVEN, R. & ZEITLIN, V. 2009 Nonlinear development of inertial instability in a barotropic shear. *Phys. Fluids* **21** (106601), 1–15.

SMYTH, W. D. & MCWILLIAMS, J. C. 1998 Instability of an axisymmetric vortex in a stably stratified, rotating environment. *Theor. Comput. Fluid Dyn.* **11**, 305–322.

SMYTH, W. D. & PELTIER, W. R. 1994 Three-dimensionalization of barotropic vortices on the f-plane. *J. Fluid Mech.* **265**, 25–64.

THORPE, S. A. 1982 On the layers produced by rapidly oscillating a vertical grid in a uniformly stratified fluid. *J. Fluid Mech.* **124**, 391–409.

YANASE, S., FLORES, C., MÉTAIS, O. & RILEY, J. J. 1993 Rotating free-shear flows. I. Linear stability analysis. *Phys. Fluids* **5** (11), 2725–2737.